

Effects of Stochastic Noises on Limit-Cycle Oscillations and Power Losses in Fusion Plasmas and Information Geometry

Rainer Hollerbach ¹  and Eun-jin Kim ^{2,*} ¹ Department of Applied Mathematics, University of Leeds, Leeds LS2 9JT, UK; r.hollerbach@leeds.ac.uk² Centre for Fluid and Complex Systems, Coventry University, Priory St, Coventry CV1 5FB, UK

* Correspondence: ejk92122@gmail.com

Abstract: We investigate the effects of different stochastic noises on the dynamics of the edge-localised modes (ELMs) in magnetically confined fusion plasmas by using a time-dependent PDF method, path-dependent information geometry (information rate, information length), and entropy-related measures (entropy production, mutual information). The oscillation quenching occurs due to either stochastic particle or magnetic perturbations, although particle perturbation is more effective in this amplitude diminishment compared with magnetic perturbations. On the other hand, magnetic perturbations are more effective at altering the oscillation period; the stochastic noise acts to increase the frequency of explosive oscillations (large ELMs) while decreasing the frequency of more regular oscillations (small ELMs). These stochastic noises significantly reduce power and energy losses caused by ELMs and play a key role in reproducing the observed experimental scaling relation of the ELM power loss with the input power. Furthermore, the maximum power loss is closely linked to the maximum entropy production rate, involving irreversible energy dissipation in non-equilibrium. Notably, over one ELM cycle, the information rate appears to keep almost a constant value, indicative of a geodesic. The information rate is also shown to be useful for characterising the statistical properties of ELMs, such as distinguishing between explosive and regular oscillations and the regulation between the pressure gradient and magnetic fluctuations.

Keywords: entropy; entropy-production; mutual information; information flow; information geometry; information length; information rate; oscillations; stochastic noise; ELMs; plasmas



Citation: Hollerbach, R.; Kim, E.-j. Effects of Stochastic Noises on Limit-Cycle Oscillations and Power Losses in Fusion Plasmas and Information Geometry. *Entropy* **2023**, *25*, 664. <https://doi.org/10.3390/e25040664>

Academic Editor: Antonio M. Scarfone

Received: 22 February 2023

Revised: 1 April 2023

Accepted: 13 April 2023

Published: 15 April 2023



Copyright: © 2023 by the authors. Licensee MDPI, Basel, Switzerland. This article is an open access article distributed under the terms and conditions of the Creative Commons Attribution (CC BY) license (<https://creativecommons.org/licenses/by/4.0/>).

1. Introduction

Stochastic noises have interesting effects on nonlinear dynamical systems, including the change in stability, noise-induced stochastic resonance [1–4], pattern formation [5], and noise-delayed extinction [6]. In particular, their dual role of stabilising an unstable equilibrium point and destabilising a stable equilibrium point can be seemingly counter-intuitive. Furthermore, given the ubiquity of oscillations in diverse fields (e.g., physics, chemistry, biology, fluid/plasmas systems, ecological systems, population dynamics, environment dynamics, etc.), the so-called oscillation quenching receives considerable attention, whereby oscillations are suppressed through oscillation death or amplitude death [4,5,7,8]. In the context of a coupled dynamical system, it can be caused by a subtle change in the coupling, such as time-delay, a parameter mismatch, etc. [9,10].

Some oscillations occurring in nature or a laboratory can be quite explosive, with the potential to cause undesirable damage to a system. An important example is quasi-periodic, limit-cycle oscillations in magnetically confined plasmas [11], such as edge-localised modes (ELMs) [12–21] and sawtooth oscillations [11]. Specifically, ELMs occur due to instabilities of pressure/current gradient at edge plasmas for a sufficiently high input power in the high-confinement mode (H-mode) regime (see, e.g., [22–25] and references therein) and take the form of sudden, quasi-periodic oscillations/bursts or more regular oscillations. The former, bursty, large-amplitude (Type I) ELMs can damage the fusion device walls, and thus

have stimulated various research efforts to suppress or mitigate such ELMs. The two main mechanisms invoke the injection of particle or magnetic field perturbations externally (e.g., resonant magnetic perturbations or a pellet injection in DIII-D, JET, ASDEX-U, EAST, KSTAR tokamaks [16,17,20]). In particular, the effect of magnetic perturbation requires attention even at a very small kinetic level [26,27].

Some of the interesting experimental observations are that the ELM suppression and mitigation depend on electron pedestal collisionality, density, edge safety factor, plasma boundary shape, as well as the characteristics of the magnetic perturbation, such as the amplitude, toroidal and poloidal mode numbers, and the amplitude/frequency of (particle) pellets [18,19]. For resonant magnetic perturbations, a stochastic layer can form on the edge, promoting rapid radial transport. However, the direct impact of stochastic magnetic fields on ELM suppression/mitigation is not well understood, given its difficulty in experimental measurements. It is thus worth studying the effect of stochastic magnetic perturbation on ELMs in simple models to gain a key understanding.

The main focus of this paper is to provide detailed study of the effects of stochastic particles and magnetic perturbations on ELMs. In our previous work [28], we proposed a stochastic ELM model based on a minimal deterministic ODE model of ELM dynamics in [12], which evolves the pressure gradient, magnetic fluctuation amplitude together with the ion radial-force balance relation where the electric fields are driven by the pressure gradient and the poloidal velocity. By varying the strength of the stochastic particle perturbation for a fixed small stochastic magnetic perturbation, we demonstrated their non-trivial effects on ELM dynamics, e.g., in altering the amplitude and period of oscillations.

In this paper, we extend the analysis in [28] and perform a systematic study by varying the strength of both stochastic external particle and magnetic perturbations to elucidate their effects on the characteristics of ELM oscillations and associated power/energy loss. We will explore a smaller value of the stochastic noise than previously considered in [28] and also scan over different strengths of these stochastic noises. In particular, we aim to address the following main questions:

- How are ELMs affected by stochastic particle and magnetic perturbation?
- Which noise is more effective in reducing the maximum power loss due to ELMs?
- How far from equilibrium is the system driven due to ELMs in the presence of the stochastic noises?
- How are power loss and energy loss due to ELMs affected by the stochastic noises and input power?
- How are power loss and energy loss due to ELMs captured by different statistical measures?
- What are robust diagnostics to identify explosive versus regular small ELMs?

In order to answer these questions, we calculate time-dependent probability density, power loss, information geometry diagnostics [29,30], and entropy-related measures [31] for different cases. Specifically, our path-dependent information geometry [25,28,32,33] allows us to quantify the changes in time-dependent PDFs along the evolution path. The entropy production rate, which measures the rate of irreversible energy dissipation in a non-equilibrium system [32,34–36], will be explored for possible links between the maximum power loss, entropy production, and information geometric diagnostics.

The remainder of this paper is organised as follows. We present our stochastic ELM model in Section 2 and a brief recap of our information geometry diagnostics and other entropy diagnostics in Section 3 to make the paper self-contained. Sections 4 and 5 provide our numerical methods and results, respectively. We conclude in Section 6. Appendix A presents the results that are not included in the main text of the paper.

2. Model

Our stochastic model of ELMs evolves two variables, x and y , which are related to the dimensionless pressure gradient p and the square-root of magnetic fluctuations E_M , respectively, as $x = p$ and $y = \sqrt{E_M}$, as follows:

$$\frac{dx}{dt} = \Phi - \tilde{D}(x)x - xy^2 + \zeta = f + \zeta, \tag{1}$$

$$\frac{dy}{dt} = \frac{1}{2}\lambda(x-1)y + \eta = g + \eta, \tag{2}$$

$$\tilde{D} = d_0 + d(x - c^2x^4)\Theta(\tilde{P} - x). \tag{3}$$

Here, $\Theta(x)$ is the Heaviside function with $\Theta(x) = 1$ for $x \geq 0$ and $\Theta(x) = 0$ for $x < 0$; \tilde{P} is the critical pressure gradient x above which turbulence is completely suppressed with no turbulent transport $d(x - c^2x^4)\Theta(\tilde{P} - x) \rightarrow 0$, where $c \equiv \tilde{P}^{-3/2}$. λ and $d_0 \ll d$ are non-negative constants. Φ is an external particle source term.

We note that Equations (1)–(3) are based on the following assumptions:

- The temperature is constant so that Φ (particle sources) plays a role as the control parameter of the energy flux (input power);
- The input power P_{in} is much greater than the critical power-threshold P_{cr} so that the electric field is mainly driven by the pressure gradient (diamagnetic velocity);
- There is no ELMy free H-mode gap;
- Time is nondimensionalised by $[(c_s/\rho_s)k\rho_s(\Delta_c^4/\rho_s^2L_p^2)]^{-1}$, where $c_s = \sqrt{T_e/m_i}$ is the ion sound speed, $\rho_s = c_s/\omega_{ci}$, ω_{ci} is the ion cyclotron frequency, and k and Δ_c are the poloidal wave number and radial correlation length of the turbulence (see [12]).

We note that the condition $P_{in} \gg P_{cr}$ above corresponds to $P_{in}/P_{cr} \gg (R\rho_sL_p^2)(\rho_s/L_p)^{1/3}$ when the pressure gradient (the diamagnetic velocity) becomes sufficiently large to dominate the contribution from the poloidal velocity. Here, R , $\rho_s = c_s/\omega_{ci}$, $c_s = \sqrt{T_e/m_i}$, ω_{ci} , L_p , and a represent the major radius, the ion Larmor radius calculated from the ion sound speed, the sound speed, the ion cyclotron frequency, the length-scale of the pressure gradient, and the minor radius, and ion sound speed, respectively [12].

In Equations (1)–(3), ζ and η are two independent Gaussian noises of strength Q_x and Q_y , with the following statistical properties

$$\begin{aligned} \langle \zeta(t)\zeta(t') \rangle &= 2Q_x\delta(t-t'), & \langle \eta(t)\eta(t') \rangle &= 2Q_y\delta(t-t'), \\ \langle \zeta(t)\eta(t') \rangle &= 0, & \langle \zeta \rangle &= \langle \eta \rangle = 0, \end{aligned} \tag{4}$$

where $\delta(t-t')$ represents a short memory time of ζ and η in comparison with any other characteristic time scales (e.g., ELM period) in the system. ζ and η in Equations (1) and (2) are included to capture any external stochastic perturbation or stochastic events/transport in the systems, such as fluctuating energy flux of unresolved scales, the outward energy flux at the edge (e.g., [37,38]), pellet pacing [16], mini-avalanches [25], stochastic magnetic fields, kinetic instabilities (due to the runaway electrons) [27], or external magnetic coils, etc. Given the uncertainty in the values of Q_x and Q_y , our interest in this paper is the trend in the effects of Q_x and Q_y on ELM dynamics.

The Fokker–Planck Equation PDF

To ensure the accurate calculation of time-dependent PDFs and information diagnostics, we will use the Fokker–Planck method [39] instead of stochastic simulations of Equations (1)–(3) [40]. Corresponding to the Langevin model in Equations (1)–(3), the Fokker–Planck equation [39] for the joint PDF $p(x, y, t)$ is given by

$$\frac{\partial p}{\partial t} = -\frac{\partial}{\partial x}(fp) - \frac{\partial}{\partial y}(gp) + Q_x\frac{\partial^2 p}{\partial x^2} + Q_y\frac{\partial^2 p}{\partial y^2} = -\partial_x J_x - \partial_y J_y. \tag{5}$$

Here,

$$f \equiv \Phi - \tilde{D}(x)x - xy^2, \quad g \equiv \frac{\lambda}{2}(x - 1)y, \tag{6}$$

$$J_x = fp - Q_x \partial_x p, \quad J_y = gp - Q_y \partial_y p, \tag{7}$$

where J_x and J_y are the probability currents of x and y .

The equations for marginal PDFs $p(x, t) = \int dy p(x, y, t)$ and $p(y, t) = \int dx p(x, y, t)$ are obtained by integrating Equation (5) over y or x , respectively

$$\frac{\partial p(x, t)}{\partial t} = -\frac{\partial}{\partial x} \int dy (fp) + Q_x \frac{\partial^2 p}{\partial x^2}, \tag{8}$$

$$\frac{\partial p(y, t)}{\partial t} = -\frac{\partial}{\partial y} \int dx (gp) + Q_y \frac{\partial^2 p}{\partial y^2}. \tag{9}$$

Here, we used the boundary conditions $J_x(x \rightarrow \pm\infty, y, t) = 0$ ($p(x \rightarrow \pm\infty, y, t) = 0$) and $J_y(x, y \rightarrow \pm\infty, t) = 0$ ($p(x, y \rightarrow \pm\infty, t) = 0$).

3. Information Geometry, Entropy Production, and Power loss

3.1. Information Rate, Length

We quantify the temporal change in PDF along its trajectory using the information rate and length. Specifically, for a one-variable system with a PDF $p(x, t)$, they are given by [25,32]

$$\Gamma^2(t) = \int dx \frac{1}{p(x, t)} \left[\frac{\partial p(x, t)}{\partial t} \right]^2, \tag{10}$$

$$\mathcal{L}(t) = \int_0^t dt_1 \Gamma(t_1).$$

We recall that in Equation (10), Γ , has units of inverse time, which quantifies the rate at which a PDF changes in time; the dimensionless $\mathcal{L}(t)$ quantifies the total cumulative change in a PDF—the total number of statistically different states that x passes through between time 0 and t . Further, we recall that for the Gaussian PDFs, $\mathcal{L}(t)$ represents the cumulative change in $p(x, t)$ measured in units of standard deviation. Given its path-dependent property of \mathcal{L} (being calculated along the PDF trajectory), it is useful for quantifying dynamical hysteresis involved in phase transitions such as the L-H transition and characterising nonlinear dynamical systems (e.g., attractors, stability/instability) [32].

For the two variables x and y , we calculate Γ and \mathcal{L} from the joint PDF $p(x, y, t)$ and $\Gamma_x, \Gamma_y, \mathcal{L}_x$, and \mathcal{L}_y from the marginal PDFs $p(x, t)$ and $p(y, t)$ as

$$\mathcal{L}(t) = \int_0^t dt_1 \Gamma(t_1), \tag{11}$$

$$\Gamma^2(t) = \int dx dy \frac{1}{p(x, y, t)} \left[\frac{\partial p(x, y, t)}{\partial t} \right]^2, \tag{12}$$

$$\mathcal{L}_x(t) = \int_0^t dt_1 \Gamma_x(t_1), \tag{13}$$

$$\mathcal{L}_y(t) = \int_0^t dt_1 \Gamma_y(t_1), \tag{14}$$

$$\Gamma_x^2(t) = \int dx \frac{1}{p(x, t)} \left[\frac{\partial p(x, t)}{\partial t} \right]^2, \tag{15}$$

$$\Gamma_y^2(t) = \int dy \frac{1}{p(y, t)} \left[\frac{\partial p(y, t)}{\partial t} \right]^2. \tag{16}$$

Utilising the invariance of Equations (13)–(16) under a (time-independent) change in variables, we will examine how x and y are correlated and self-regulated (e.g., [25,33]) in explosive versus small ELMs in Section 5.4. Note that, in our model, x and y are dependent on $\Gamma^2 \neq \Gamma_x^2 + \Gamma_y^2$.

3.2. Entropy, Entropy Production, and Entropy Flow

We recall differential entropies S_x , S_y , and S based on the marginal PDFs $p(x, t)$ and $p(y, t)$ and the joint PDF $p(x, y, t)$, respectively, and mutual entropy I as follows [31,32]:

$$S_x = - \int dx p(x, t) \ln(p(x, t)), \tag{17}$$

$$S_y = - \int dy p(y, t) \ln(p(y, t)), \tag{18}$$

$$S = - \int dx dy p(x, y, t) \ln(p(x, y, t)), \tag{19}$$

$$I = S_x + S_y - S = \int dx dy p(x, y, t) \ln \frac{p(x, y, t)}{p(x, t)p(y, t)}. \tag{20}$$

As a measure of irreversibility, we consider the total entropy production

$$\dot{S}_T = \dot{S} + \dot{S}_m, \tag{21}$$

where \dot{S}_m is the entropy flow rate (entropy flux to the environment at temperature Q_x and Q_y), and the two terms are defined by

$$\dot{S}_T = \int dx dy \left[\left(\frac{1}{Q_x p} J_x^2 + \frac{1}{Q_y p} J_y^2 \right) \right], \quad \dot{S}_m = \int dx dy \left[\left(\frac{1}{Q_x} J_x f + \frac{1}{Q_y} J_y g \right) \right]. \tag{22}$$

It is important to note that \dot{S}_T and \dot{S}_m in Equation (22) are calculated from a joint PDF, and can be shown to take the following form

$$\dot{S}_T = \dot{S}_{Tx} + \dot{S}_{Ty}, \tag{23}$$

$$\dot{S}_m = \dot{S}_{mx} + \dot{S}_{my}, \tag{24}$$

where

$$\dot{S}_{Tx} = \int dx dy \frac{1}{Q_x p} J_x^2, \quad \dot{S}_{Ty} = \int dx dy \frac{1}{Q_y p} J_y^2, \tag{25}$$

$$\dot{S}_{mx} = \int dx dy \frac{1}{Q_x} J_x f, \quad \dot{S}_{my} = \int dx dy \frac{1}{Q_y} J_y g. \tag{26}$$

\dot{S}_{Tx} and \dot{S}_{Ty} (\dot{S}_{mx} and \dot{S}_{my}) represent the entropy production rates in x and y (entropy x and y to their heat baths), respectively.

For independent x and y we have that $\dot{S}_{Tx} = \dot{S}_x + \dot{S}_{mx}$ and $\dot{S}_{Ty} = \dot{S}_y + \dot{S}_{my}$, but in general, these do not hold due to the interaction between x and y . These relations, therefore, need to be generalised as follows [28]:

$$\dot{S}_{Tx} = \dot{S}_x + \dot{S}_{mx} - T_{y \rightarrow x}, \quad \dot{S}_{Ty} = \dot{S}_y + \dot{S}_{my} - T_{x \rightarrow y}. \tag{27}$$

Here, $T_{x \rightarrow y}$ and $T_{y \rightarrow x}$ are the information rate from x to y and y to x , respectively, given by

$$T_{y \rightarrow x} = \partial_\tau I(x(t + \tau), y(t))|_{\tau=0} = - \int dx dy J_x(x, y, t) \partial_x \ln \left[\frac{p(x, t)}{p(x, y, t)} \right], \tag{28}$$

$$T_{x \rightarrow y} = \partial_\tau I(x(t), y(t + \tau))|_{\tau \rightarrow 0} = - \int dx dy J_y(x, y, t) \partial_y \ln \left[\frac{p(y, t)}{p(x, y, t)} \right], \quad (29)$$

where I is the mutual information in Equation (20). It is emphasised that the rate at which the mutual information changes in time is the sum of $T_{x \rightarrow y}$ and $T_{y \rightarrow x}$ (see [28]):

$$\frac{dI}{dt} = T_{y \rightarrow x} + T_{x \rightarrow y}. \quad (30)$$

3.3. Power Loss

One of the useful measures in fusion plasmas is the power loss P_L representing how much power is lost through turbulent transport

$$P_L = \Phi - \left\langle \frac{dx}{dt} \right\rangle = \langle \tilde{D}(x)x + xy^2 \rangle. \quad (31)$$

To be able to quantify how explosive the power loss is compared to the input power, we define a normalised power loss as

$$\overline{P}_L = \frac{P_L}{\Phi}, \quad (32)$$

and use it to compare different cases in examining the effect of stochastic noises in Section 5.

4. Numerical Experiments

We numerically solve the Fokker–Planck Equations (5)–(7) by discretising x and y using second-order finite differences [28] with the resolution $\sim 10^{-3}$ in x and y . For time-stepping, we use the second-order Runge–Kutta with time steps as small as 2×10^{-5} . We look for the symmetric solutions $p(x, y, t) = p(x, -y, t)$ in y on physical basis and solve Equations (5)–(7) in a 2D-box in $x = [x_{min}, x_{max}]$ and $y = [0, y_{max}]$ with the boundary conditions $p(x_{min}, y, t) = p(x_{max}, y, t) = p(x, y_{max}, t) = 0$, and $\frac{\partial p}{\partial y} = 0$ at $y = 0$. x_{min} , x_{max} , and y_{max} are chosen to ensure that the solution becomes sufficiently small at the boundaries of the 2D-box, in particular, the total probability $\iint p(x, y, t) dx dy = 1$ to within 10^{-4} .

Since the purpose of this paper is to investigate the effect of stochastic noises Q_x and Q_y on oscillations at different values of Φ/d , we fix an initial condition to be a narrow Gaussian PDF with the mean values $\langle x(0) \rangle = 1.2$ and $\langle y(0) \rangle = 0.2$ and standard deviations $\sigma_x(0) = \sigma_y(0) = 0.04$ while keeping the parameters $d_0 = 10^{-3}$, $d = 0.1$, $\tilde{P} = 1.05$, and $\lambda = 5$. We consider the four different values $\Phi/d = 0.6, 0.8, 1.0, 1.2$. Recall that in the deterministic model, as Φ/d is increased from $\Phi/d = 0.4$ to 1.2, ELMs gradually change from explosive events (giant ELMs) to more sinusoidal (grassy, small ELMs) with a shorter oscillation period. For each Φ/d , we vary the values of $Q_x, Q_y = 3 \times 10^{-6}, 10^{-5}, 3 \times 10^{-5}, 10^{-4}, 3 \times 10^{-4}, 10^{-3}$.

5. Results

The previous work [28] fixed Q_y , and explored the effects of Q_x and showed that random trajectories due to stochastic noise-induced phase-mixing where phase information is lost over time. Consequently, in the long time limit, $p(x, y, t)$ will completely forget the phase information as well as the initial conditions and will reach a stationary PDF regardless of the initial conditions. In other words, in the stationary state, oscillations are completely suppressed with equal probability of all different phases. Furthermore, there was some indication of shortening the period of oscillation for a more explosive oscillation. In the following, we examine the results for different values of Q_x and Q_y .

5.1. ODE Solution

We start by looking at the ODE solution to appreciate the difference between the four cases $\Phi/d = 0.6, 0.8, 1.0, 1.2$. Figure 1 shows the time-evolution of $x = P$ and $y = \sqrt{E_M}$ in Equations (1)–(3) in the absence of noise $\zeta = \eta = 0$. It can easily be seen that the period of ELMs becomes smaller for larger Φ . For the smallest $\Phi/d = 0.6$, x (in red) slowly rises before suddenly collapsing back to a small value. This is triggered by the onset of the burst (spike) of y (in blue) due to the instability of the L-mode solution ($x < 1, y = 0$). Between the bursts, y spends a long time around the unstable L-mode solution ($x < 1, y = 0$). We also see that the oscillations for larger Φ/d become more regular/sinusoidal and more symmetric. Figure 2 shows the normalised power loss \bar{P}_L defined in Equation (32) for the deterministic cases shown in Figure 1.

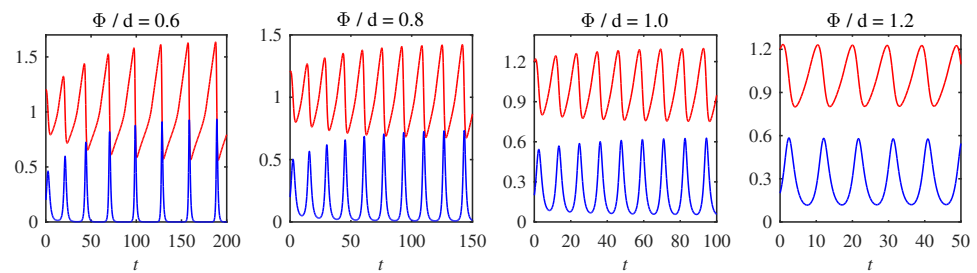


Figure 1. Deterministic solutions of Equations (1)–(3), with $\zeta = \eta = 0$ and initial conditions $x = 1.2$ and $y = 0.2, d_0 = 10^{-3}, d = 0.1, \bar{P} = 1.05, \lambda = 5$, and $\Phi/d = 0.6, 0.8, 1.0, 1.2$ as indicated above each panel. Red denotes $x = P$, blue $y = \sqrt{E_M}$.

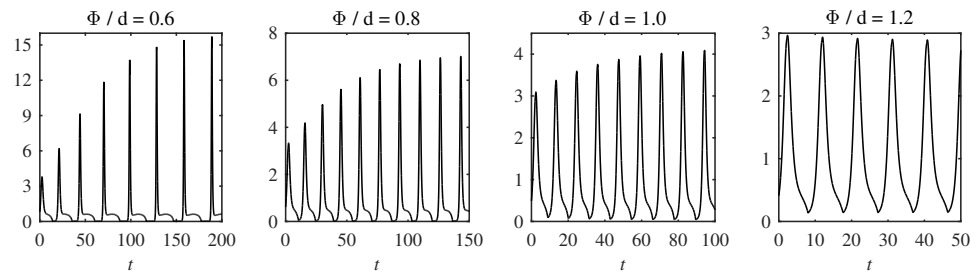


Figure 2. Normalised power loss against time for the deterministic solutions in Figure 1 for $\Phi/d = 0.6, 0.8, 1.0, 1.2$.

5.2. Mean and Standard Deviation

For non-zero stochastic noises, we show time traces of $\langle x \rangle, \langle y \rangle, \sigma_x$, and σ_y , for the smallest and largest values of $\Phi/d = 0.6, 1.2$ in Figures 3–6 here, while those for $\Phi/d = 0.8, 1.0$ in Appendix A (Figures A1–A4). Each plot contains results for different values of $Q_x [Q_y] = 3 \times 10^{-6}$ in red, 10^{-5} in blue, 3×10^{-5} in green, 10^{-4} in black, 3×10^{-4} in sky-blue, and 10^{-3} in magenta, for fixed $Q_y [Q_x] = 10^{-5}$.

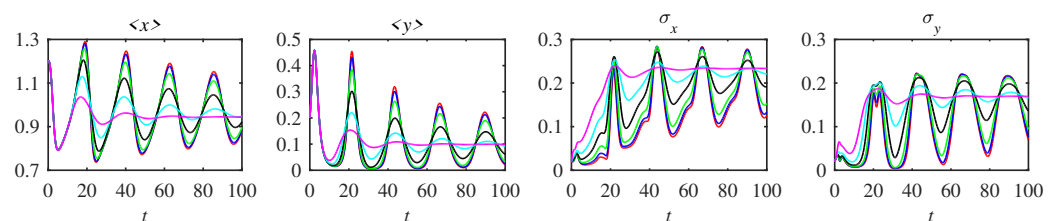


Figure 3. $\Phi/d = 0.6$: Scan over $Q_x = 3 \times 10^{-6}, 10^{-5}, 3 \times 10^{-5}, 10^{-4}, 3 \times 10^{-4}, 10^{-3}$ for $Q_y = 10^{-5}$.

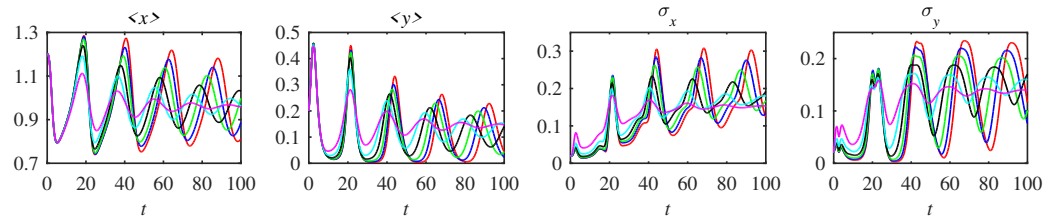


Figure 4. $\Phi/d = 0.6$: Scan over $Q_y = 3 \times 10^{-6}, 10^{-5}, 3 \times 10^{-5}, 10^{-4}, 3 \times 10^{-4}, 10^{-3}$ for $Q_x = 10^{-5}$.

Overall, for all values of Q_x, Q_y , the increase in the standard deviation over time is observed due to phase-mixing, while the amplitude of quasi-periodic oscillations gradually decreases over time. This oscillation quenching occurs more rapidly for larger values of Q_x or Q_y , and is more pronounced in the evolution of $\langle y \rangle$ than that of $\langle x \rangle$, probably because the instability (of y) is more susceptible to stochastic noises. Further, compared with Q_y , Q_x is more effective at quenching oscillation amplitude.

For $\Phi/d = 0.6$, in comparison with Figure 1, the uncertainty induced by the stochastic noise ($Q_x, Q_y \neq 0$) inhibits y from becoming smaller than a certain value depending on Q_x and Q_y . As a result, oscillations become less explosive, as can be seen in Figures 3 and 4. On the other hand, the period of oscillation tends to become smaller for larger values of Q_x or Q_y . A close comparison of the cases with varying Q_x and Q_y for $\Phi/d = 0.6$ reveals that such shortening of the period is more pronounced for increasing Q_y for fixed Q_x (Figure 4) compared with the case of increasing Q_x for fixed Q_y (Figure 3).

A similar trend persists for $\Phi/d = 0.8$ (see Figures A1 and A2), although the period of oscillation is shortened to a lesser degree in comparison to the case of $\Phi/d = 0.6$. This, together with the observation made above, indicates that Q_x induces a more severe amplitude quenching while Q_y is more effective at shortening the oscillation period, respectively.

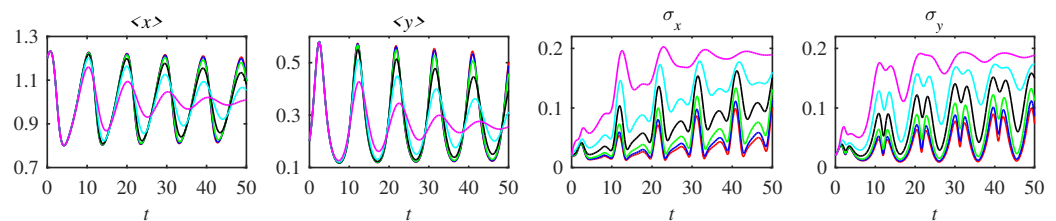


Figure 5. $\Phi/d = 1.2$: Scan over $Q_x = 3 \times 10^{-6}, 10^{-5}, 3 \times 10^{-5}, 10^{-4}, 3 \times 10^{-4}, 10^{-3}$ for $Q_y = 10^{-5}$.

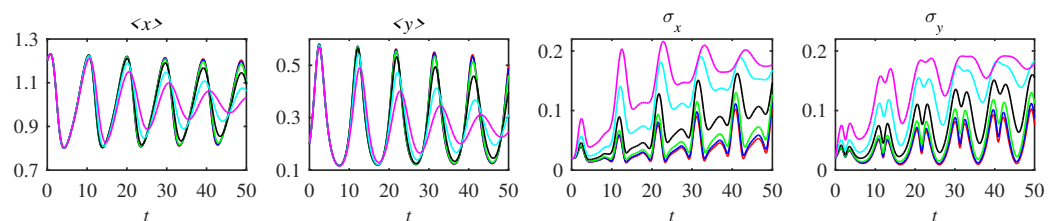


Figure 6. $\Phi/d = 1.2$: Scan over $Q_y = 3 \times 10^{-6}, 10^{-5}, 3 \times 10^{-5}, 10^{-4}, 3 \times 10^{-4}, 10^{-3}$ for $Q_x = 10^{-5}$.

In contrast, for $\Phi/d = 1.2$ in Figures 5 and 6, Q_x and Q_y now act in such a way to increase the period rather than decrease it. (A similar tendency can be seen for $\Phi/d = 1.0$ in Figures A3 and A4.) This is due to the main difference in oscillation characteristics for $\Phi/d = 0.6$ and 1.2. Specifically, for $\Phi/d = 0.6$, the oscillations occur less frequently and are explosive, and stochastic noise can turn such rare, explosive oscillations (large ELMs) into more frequent small events (small ELMs). On the other hand, for $\Phi/d = 1.2$, oscillations are more regular, being more similar to linear oscillations where a stochastic noise can reduce the oscillation frequency through damping.

5.3. Power Loss

We observed that in the long time limit, $P_L \rightarrow \Phi$ in all cases. Thus, the normalised power loss $\bar{P}_L = P_L/\Phi$ in Equation (32) gives us a useful measure for comparing different cases of Φ . The normalised power loss \bar{P}_L is shown in Figure 7 for different cases. The upper [lower] panel shows the results for different values of Q_x [Q_y] = 3×10^{-6} in red, 10^{-5} in blue, 3×10^{-5} in green, 10^{-4} in black, 3×10^{-4} in sky-blue, and 10^{-3} in magenta for Q_y [Q_x] = 10^{-5} , respectively, so using the same colour scheme as before.

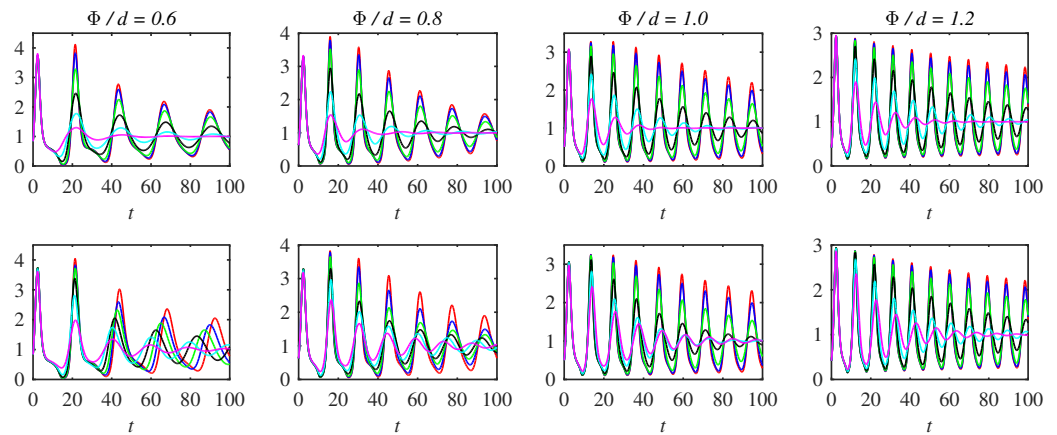


Figure 7. Normalised power loss \bar{P}_L for $\Phi/d = 0.6, 0.8, 1.0, 1.2$ from left to right: Scan over Q_x [Q_y] = $3 \times 10^{-6}, 10^{-5}, 3 \times 10^{-5}, 10^{-4}, 3 \times 10^{-4}, 10^{-3}$ for Q_y [Q_x] = 10^{-5} in the upper [lower] row.

Overall, the smaller Φ/d is, the larger the excursion of the normalised power from unity, with larger maxima and smaller minima, similar to what was observed in the deterministic case in Figure 2. This manifests a more explosive nature of the oscillations for smaller Φ . Compared with the deterministic case, the stochastic noise reduces the peak power loss, $\bar{P}_L^m = \max(\bar{P}_L)$, yielding a smaller \bar{P}_L^m for larger Q_x and Q_y . Other notable main effects of stochastic noise Q_x and Q_y seen in Figures 2 and 7 are as follows. First, as time increases, the peak value and oscillation amplitude of \bar{P}_L decrease, similar to what was observed in the mean values (Figures 3–6). Second, for a given Φ , the peak value \bar{P}_L monotonically decreases as either Q_x or Q_y increases. A more significant reduction in the maximum power loss is observed as Q_x increases for a fixed Q_y (the upper row in Figure 7), compared with the other case of increasing Q_y for fixed Q_x (the lower row in Figure 7). For instance, for $\Phi/d = 0.6$, the values of the second peaks (just beyond $t = 20$) in power loss in Figure 7 are

$$\begin{aligned} \bar{P}_L^m &= (4.11, 3.82, 3.28, 2.46, 1.77, 1.30) \text{ as } Q_x \text{ varies,} \\ \bar{P}_L^m &= (4.04, 3.82, 3.72, 3.38, 2.81, 1.98) \text{ as } Q_y \text{ varies.} \end{aligned} \tag{33}$$

Third, the effects of stochastic noise, noted above, tend to be more pronounced for smaller Φ . This means that the stochastic noises tend to be very effective in quickly suppressing the large power loss associated with large ELMs ($\Phi/d = 0.6$). Finally, Q_x and Q_y shorten [lengthen] the period of the P_L oscillations in the case of small $\Phi/d = 0.6, 0.8$ [large $\Phi/d = 1.0, 1.2$].

Fourth, the time averages of the normalised \bar{P}_L^m take values ranging from 1.05 for $\Phi/d = 0.6$ to 1.02 for $\Phi/d = 1.2$, with some differences at the level of a few per cent. This suggests that the input power Φ is a reasonable estimate of the time average of P_L . However, as noted above, very large fluctuations in P_L about the average values (see Figure 7) occur for more explosive cases ($\Phi/d = 0.6$), leading to increased power loss due to ELMs.

To demonstrate how Q_x and Q_y reduce the energy loss W_{ELM} caused by such ELMs, we approximate W_{ELM} by the time-integral of the power loss that is larger than the input power Φ as

$$W_{ELM}/\Phi \sim (\Delta t)(\bar{P}_L^m - 1)/2, \tag{34}$$

where Δt is the duration of the ELM, approximated by the distance between the times where $\bar{P}_L = 1$. The factor of 1/2 accounts for the fact that the peak has a roughly triangular shape going up and down, so estimating W_{ELM}/Φ as the area of the rectangle $(\Delta t)(\bar{P}_L^m - 1)$ would clearly be an over-estimate.

For instance, we again consider the second oscillation peaks in power loss for the case $\Phi/d = 0.6$ in Figure 7, and extract that:

$$\begin{aligned} \Delta t &= (5.65, 5.93, 6.59, 8.03, 9.66, 11.31) \text{ as } Q_x \text{ varies,} \\ \Delta t &= (5.72, 5.93, 5.96, 6.10, 6.51, 7.53) \text{ as } Q_y \text{ varies.} \end{aligned} \tag{35}$$

Using Equations (33) and (35) in Equation (34) then yields:

$$\begin{aligned} W_{ELM}/\Phi &= (8.8, 8.4, 7.5, 5.9, 3.7, 1.7) \text{ as } Q_x \text{ varies,} \\ W_{ELM}/\Phi &= (8.7, 8.4, 8.1, 7.3, 5.9, 3.9) \text{ as } Q_y \text{ varies.} \end{aligned} \tag{36}$$

Figure 8 shows these quantities in Equations (33), (35) and (36), with red [blue] corresponding to Q_x [Q_y] being the noise that is varying. Both \bar{P}_L^m and W_{ELM}/Φ in panels (a) and (c) are seen to decrease as Q_x and Q_y increase, with a greater reduction due to Q_x compared to Q_y . In comparison, Δt has the opposite tendency, its value increasing with Q_x and Q_y , with a more dominant effect of Q_y .

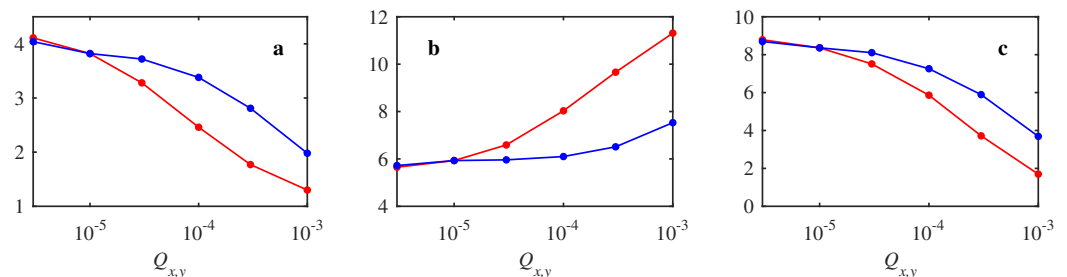


Figure 8. $\Phi/d = 0.6$: Panel (a) shows \bar{P}_L^m from Equation (33), panel (b) shows Δt from Equation (35), and panel (c) shows W_{ELM}/Φ from Equation (36). The horizontal axis is Q_x [Q_y] for the red [blue] curves, corresponding to Q_x [Q_y] varying while the other noise is kept fixed at 10^{-5} .

Finally, we check on the experimental observation that the power loss due to ELMs remains a constant fraction of the input power, $W_{ELM} \cdot f_{ELM} = \{0.3 - 0.4\} \times \Phi$, where f_{ELM} is the frequency of ELMs [18,19]. To this end, we focus on the red curves in Figure 7, having $Q_x = 3 \times 10^{-6}$, $Q_y = 10^{-5}$ in the top row and $Q_x = 10^{-5}$, $Q_y = 3 \times 10^{-6}$ in the bottom row. We use the second oscillations in each case to extract \bar{P}_L^m and Δt , which then allows us to calculate W_{ELM}/Φ . The next few oscillations give us the period T_{ELM} , so then $f_{ELM} = 1/T_{ELM}$ gives us the final ingredient to compute the desired quantity $(W_{ELM}/\Phi)f_{ELM}$.

The first four rows in Table 1 use data from the top row of Figure 7, so $Q_x = 3 \times 10^{-6}$, $Q_y = 10^{-5}$. The next four rows use data from the bottom row of Figure 7, so $Q_x = 10^{-5}$, $Q_y = 3 \times 10^{-6}$. The final four rows use data from Figure 2, so the deterministic system with $Q_x = Q_y = 0$. We can see that even quite small amounts of noise reduce the power loss, especially at the smaller Φ/d values where we obtain giant ELMs. For larger noise levels, the reduction in W_{ELM} and, thus, also the power loss becomes even greater, as seen previously in Figure 8.

However, despite such dependence of W_{ELM}/Φ on Q_x , Q_y , and Φ , the power loss due to ELMs $(W_{ELM}/\Phi)f_{ELM}$ in the last column in Table 1 is within the range of 0.33–0.39,

well consistent with the experimental observation 0.3–0.4 [18,19] noted above. In contrast, for a deterministic system (shown in Figure 2), this is no longer the case since $(W_{ELM}/\Phi)f_{ELM} = 0.33\text{--}0.75$, taking the value 0.75 for the large ELM $\Phi/d = 0.6$. These results thus suggest that the presence of stochastic noise is essential for reproducing the experimental results.

Table 1. Calculations of the relative power loss $(W_{ELM}/\Phi)f_{ELM}$, as described in the text.

Φ/d	\bar{P}_L^m	Δt	W_{ELM}/Φ	T_{ELM}	$(W_{ELM}/\Phi)f_{ELM}$
0.6	4.11	5.65	8.8	22.8	0.39
0.8	3.89	4.08	5.9	15.6	0.38
1.0	3.27	3.69	4.2	11.6	0.36
1.2	2.88	3.42	3.2	9.6	0.33
0.6	4.04	5.72	8.7	23.7	0.37
0.8	3.82	4.13	5.8	15.6	0.37
1.0	3.25	3.71	4.2	11.6	0.36
1.2	2.87	3.43	3.2	9.6	0.33
0.6	15.71	3.07	22.6	30.3	0.75
0.8	7.10	3.31	10.1	16.7	0.60
1.0	4.15	3.41	5.4	11.8	0.46
1.2	2.87	3.40	3.2	9.6	0.33

5.4. Information Rate

We now examine how the different types of oscillations are reflected in the information geometry, in particular, how the correlation between x and y inherent in oscillations is captured. Figures 9 and 10 show the time traces of $\Gamma_x, \mathcal{L}_x, \Gamma_y,$ and \mathcal{L}_y for different cases of parameter scanning for $\Phi/d = 0.6$, while Figures 11 and 12 are for $\Phi/d = 1.2$ (See Figures A5–A8 for $\Phi/d = 0.8, 1.0$.) In all cases, it is clearly seen that the larger Q_x or Q_y , the smaller $\Gamma_x, \Gamma_y, \mathcal{L}_x,$ and \mathcal{L}_y . This is because larger stochastic noise makes the number of statistically distinguishable states smaller. Comparing the upper and lower panels in all cases, Q_x seems to cause more decrease in \mathcal{L}_x and \mathcal{L}_y compared with Q_y due to Q_x 's stronger oscillation quenching.

Although the fine features of Γ_x and Γ_y are a bit different (e.g., with different oscillation periods), the overall evolution of \mathcal{L}_x and \mathcal{L}_y is remarkably similar, suggesting that x and y undergo similar changes in statistical states despite their different evolutions. To further quantify this correlation, Figures 13 and 14 plot the information phase-portrait, which plots Γ_y against Γ_x . The diagonal line $\Gamma_x = \Gamma_y$ is overplotted as the black solid line. The oscillation around $\Gamma_x = \Gamma_y$ reveals a regulatory interaction between x and y as a result of overshooting (due to inertial) and restoring forces (due to interaction). Recall that when Γ_x and Γ_y cross each other, the time scales of x and y match with a perfect balance. Such regulatory behaviour is most prominent in the case of $\Phi/d = 1.2$ in Figure 14; the large deviation from $\Gamma_x = \Gamma_y$ in Figure 13 is due to explosive oscillation (intermittency) as well as initial transients. Finally, the larger Q_x and Q_y are, the less prominent the crossing between Γ_x and Γ_y due to loss of phase information (See Figures A9 and A10 for $\Phi/d = 0.8, 1.0$.)

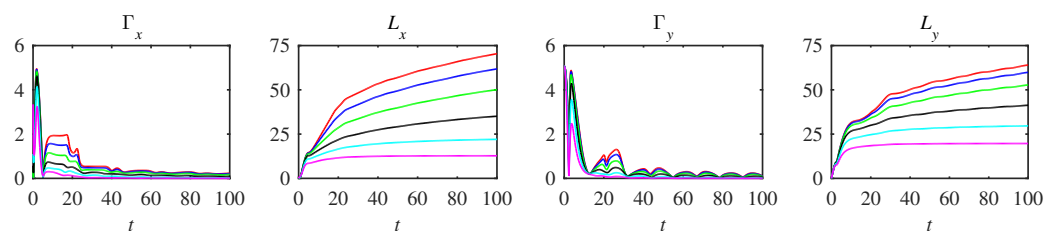


Figure 9. $\Phi/d = 0.6$: Scan over $Q_x = 3 \times 10^{-6}, 10^{-5}, 3 \times 10^{-5}, 10^{-4}, 3 \times 10^{-4}, 10^{-3}$ for $Q_y = 10^{-5}$.

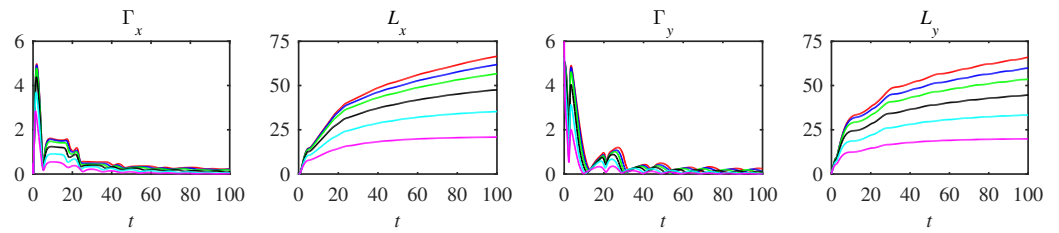


Figure 10. $\Phi/d = 0.6$: Scan over $Q_y = 3 \times 10^{-6}, 10^{-5}, 3 \times 10^{-5}, 10^{-4}, 3 \times 10^{-4}, 10^{-3}$ for $Q_x = 10^{-5}$.

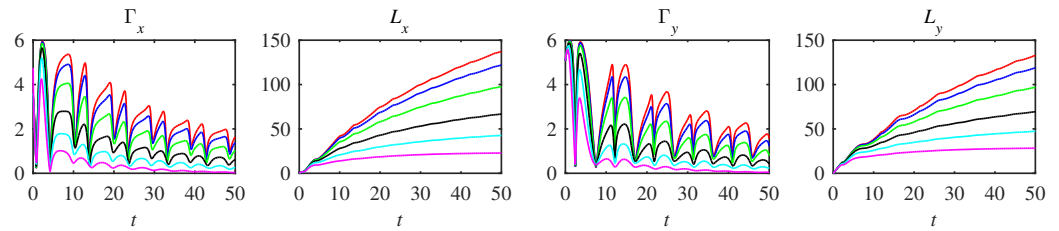


Figure 11. $\Phi/d = 1.2$: Scan over $Q_x = 3 \times 10^{-6}, 10^{-5}, 3 \times 10^{-5}, 10^{-4}, 3 \times 10^{-4}, 10^{-3}$ for $Q_y = 10^{-5}$.

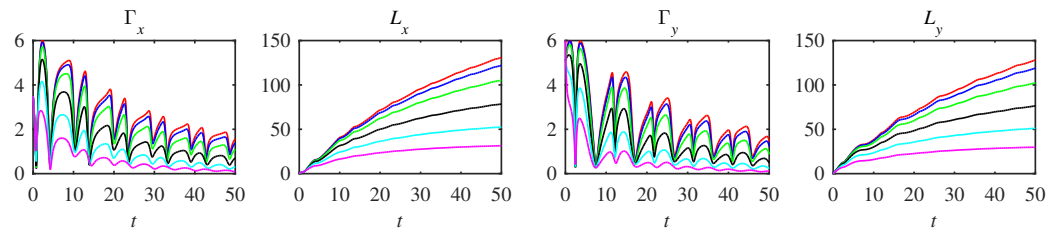


Figure 12. $\Phi/d = 1.2$: Scan over $Q_y = 3 \times 10^{-6}, 10^{-5}, 3 \times 10^{-5}, 10^{-4}, 3 \times 10^{-4}, 10^{-3}$ for $Q_x = 10^{-5}$.

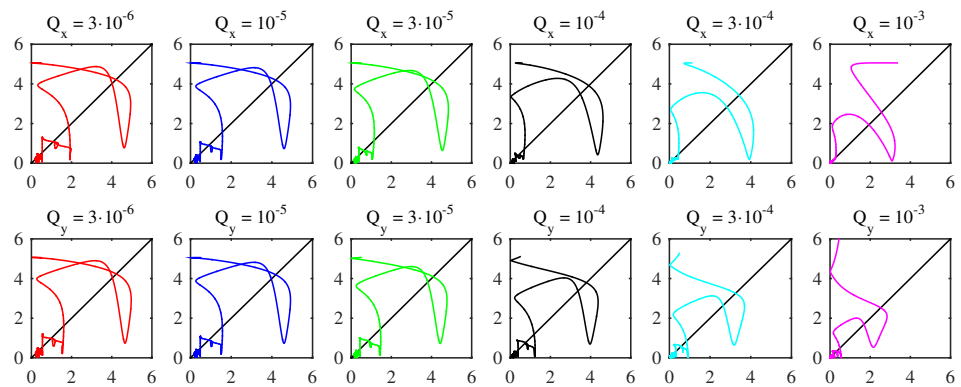


Figure 13. $\Phi/d = 0.6$: Γ_x on the x -axis versus Γ_y on the y -axis. The top row shows scans of Q_x as indicated at fixed $Q_y = 10^{-5}$; the bottom row shows scans of Q_y as indicated at fixed $Q_x = 10^{-5}$.

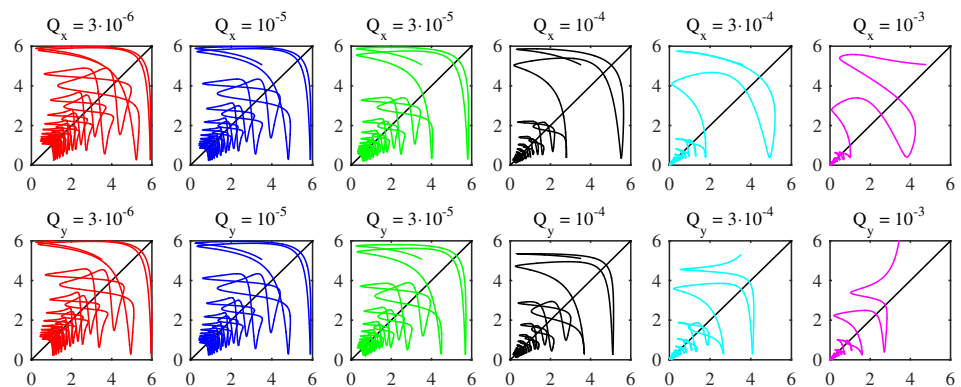


Figure 14. $\Phi/d = 1.2$: Γ_x on the x -axis versus Γ_y on the y -axis. The top row shows scans of Q_x as indicated at fixed $Q_y = 10^{-5}$; the bottom row shows scans of Q_y as indicated at fixed $Q_x = 10^{-5}$.

5.5. Entropy Production

In both Figures 15 and 16, Panels a and b show \dot{S}_{Tx} and \dot{S}_{Ty} , respectively, as functions of time when scanning over Q_x at fixed $Q_y = 10^{-5}$; Panels c and d show \dot{S}_{Tx} and \dot{S}_{Ty} , respectively, as functions of time when scanning over Q_y at fixed $Q_x = 10^{-5}$. What is prominent is that \dot{S}_{Tx} and \dot{S}_{Ty} in Panels a and d decrease as Q_x, Q_y are increased, whereas \dot{S}_{Ty} and \dot{S}_{Tx} in Panels b and c do not show this tendency. That is, for a smaller value of Q_x , \dot{S}_{Tx} becomes larger while \dot{S}_{Tx} changes much less, and vice versa. Mathematically, this appears because \dot{S}_{Tx} has Q_x in its denominator while \dot{S}_{Ty} has Q_y in its denominator; $Q_x \dot{S}_{Tx}$ would be less subject to change when Q_x changes. (If x were an independent Gaussian variable, $\Gamma_x^2 = Q_x \dot{S}_{Tx} / \sigma_x^2 + \dot{S}_x^2$). Further, it is useful to note that this different behaviour of \dot{S}_{Tx} [\dot{S}_{Ty}] upon the change in Q_x [Q_y] sharply contrasts with the similar behaviour of Γ_x and Γ_y in Figures 13 and 14. These results appear to be another manifestation that the geometric measures, such as Γ_x and Γ_y , better capture the correlations between x and y , as discussed in Section 5.4 above.

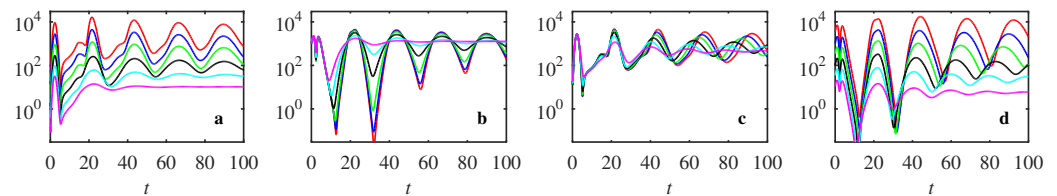


Figure 15. $\Phi/d = 0.6$: Panels (a and b) show \dot{S}_{Tx} and \dot{S}_{Ty} , respectively, as functions of time when scanning over Q_x at fixed $Q_y = 10^{-5}$. Panels (c and d) show \dot{S}_{Tx} and \dot{S}_{Ty} , respectively, as functions of time when scanning over Q_y at fixed $Q_x = 10^{-5}$.

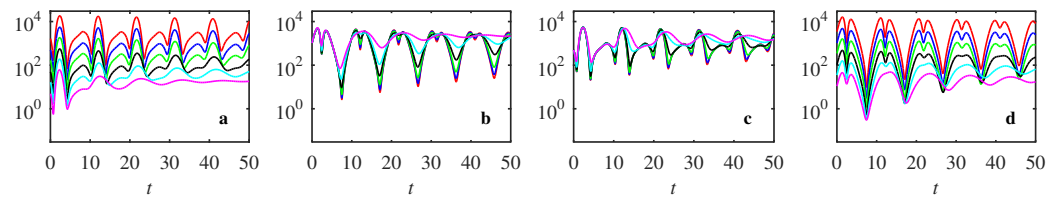


Figure 16. $\Phi/d = 1.2$: Panels (a and b) show \dot{S}_{Tx} and \dot{S}_{Ty} , respectively, as functions of time when scanning over Q_x at fixed $Q_y = 10^{-5}$. Panels (c and d) show \dot{S}_{Tx} and \dot{S}_{Ty} , respectively, as functions of time when scanning over Q_y at fixed $Q_x = 10^{-5}$.

5.6. Comparison among Power Loss, Information Rate, and Entropy Production

We considered the individual information rates Γ_x and Γ_y calculated from the marginal PDFs of x and y in Section 5.4 and the individual components of entropy production rate \dot{S}_{Tx} and \dot{S}_{Ty} in Section 5.5. One key difference between these measures was noted that Γ_x is reduced somewhat similarly as either Q_x or Q_y increases, while \dot{S}_{Tx} is more severely reduced by Q_x than Q_y . In this section, we examine the statistical measure of the total system by calculating the information rate Γ from joint PDFs (see Equation (17)) and the total entropy production rates $\dot{S}_T = \dot{S}_{Tx} + \dot{S}_{Ty}$ (see Equation (23)) and compare them with the power loss in Section 5.3. The results are shown in Figures 17 and 18, respectively, for those cases corresponding to Figure 7.

Notably, Figure 17 exhibits a stair-case-like evolution in time where each large power loss during one ELM oscillation is associated with a region of an almost constant Γ , the value of Γ suddenly decreases from one oscillation to another. If this constant Γ is to be interpreted as a geodesic [32], which was advocated as a signature of self-organisation, ELMs in the presence of stochastic noises can be viewed to occur by jumping from one self-organised state to another.

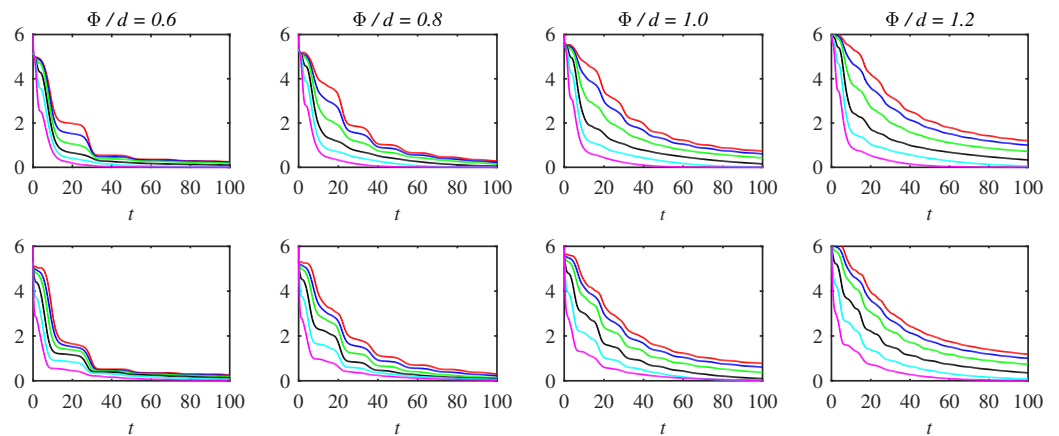


Figure 17. Information rate Γ for $\Phi/d = 0.6, 0.8, 1.0, 1.2$ from left to right: Scan over $Q_x [Q_y] = 3 \times 10^{-6}, 10^{-5}, 3 \times 10^{-5}, 10^{-4}, 3 \times 10^{-4}, 10^{-3}$ for $Q_y [Q_x] = 10^{-5}$ in the upper [lower] row.

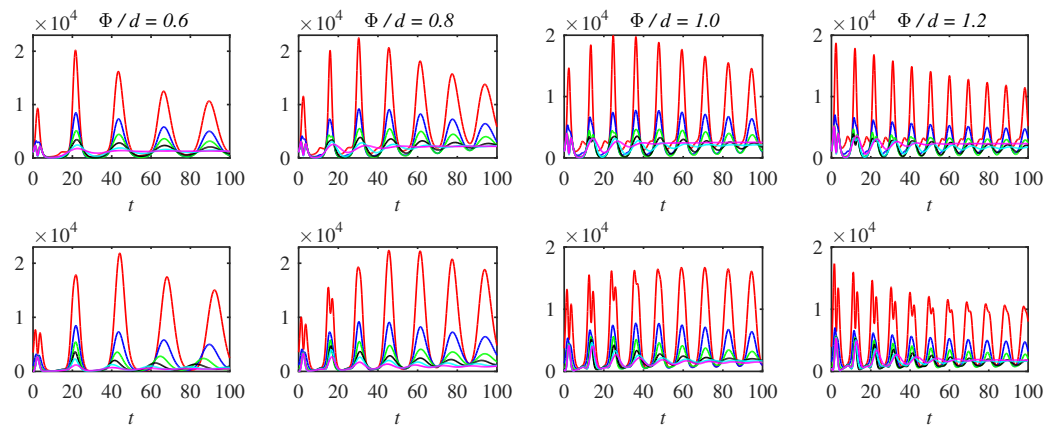


Figure 18. The total entropy production rate \dot{S}_T for $\Phi/d = 0.6, 0.8, 1.0, 1.2$ from left to right: Scan over $Q_x [Q_y] = 3 \times 10^{-6}, 10^{-5}, 3 \times 10^{-5}, 10^{-4}, 3 \times 10^{-4}, 10^{-3}$ for $Q_y [Q_x] = 10^{-5}$ in the upper [lower] row.

On the other hand, the overall behaviour of the total entropy production rate \dot{S}_T in Figure 18 is seen to be well-correlated with that of the power loss in Figure 7, with the maxima of \dot{S}_T and \bar{P}_L occurring at similar times, although in some cases, especially for $Q_y < Q_x$, \dot{S}_T shows double peaks in the early evolution.

6. Conclusions

We conducted a detailed investigation into the effects of various stochastic noises on the statistical properties of ELMs using a time-dependent PDF method and path-dependent information geometry (information rate, information length). Overall, the amplitude of oscillation is diminished over time through the phase-mixing of different trajectories due to either stochastic particle or magnetic perturbations. However, particle perturbation is more effective in this amplitude diminishment compared with magnetic perturbations. In regards to the effects on oscillation frequency, the stochastic noise acts to increase the frequency of more explosive oscillations (large ELMs), while it decreases the frequency of more sinusoidal regular oscillations (small ELMs). In both cases, magnetic perturbations are more effective at altering the oscillation period.

We provided a detailed study of how power loss is affected in different cases. Most of all, a dramatic decrease in power loss for explosive ELMs (small Φ) was observed as Q_x and Q_y increase, with a more significant effect of Q_x . The peak power loss and the energy loss due to ELMs were estimated for different Φ , Q_x , and Q_y , revealing the important effect of stochastic noises on reducing such losses. However, despite the reduction in W_{ELM}/Φ by Q_x and Q_y and their dependence on Φ , the power loss due to ELMs $(W_{ELM}/\Phi)_{f_{ELM}}$ (in Table 1) for all cases gives 0.33–0.37, consistent with the experimental observation [18,19].

In contrast, for a deterministic system, a deviation from this relation was found for large ELMs. These highlight the importance of a stochastic ELM model for reproducing the experimental results.

Furthermore, the power loss was shown to be strongly correlated with the total entropy production, indicating that the maximum power loss involves a large, irreversible energy dissipation in non-equilibrium. Despite such a strongly non-equilibrium evolution, each ELM oscillation seems to occur in a state where the information rate Γ (calculated from a joint PDF) is almost constant, suggesting a geodesic-like behaviour (see [32] and references therein) over one ELM cycle. Envisioning the latter to be a signature of self-organisation Γ [32], the time evolution of ELMs in the presence of stochastic noises is proposed to consist of a sequence of sudden transitions between the different self-organised states.

Another utility of the information geometry in capturing the ELM dynamics is further discussed. Specifically, a strong coupling between x and y in more regular oscillation is captured by a similar evolution of \mathcal{L}_x and \mathcal{L}_y , despite the differences in the details of the time-evolutions of the two variables [33]. Furthermore, the information phase-portrait (Γ_x versus Γ_y) shows that a strong coupling between x and y can be measured by the oscillation of Γ_x and Γ_y around $\Gamma_x = \Gamma_y$, suggesting the time competition in statistical space. It was also suggested that the correlation is better measured by these information geometric measures than the entropy production rates \dot{S}_{Tx} and \dot{S}_{Ty} that are affected differently by stochastic noise.

It will be of interest to further extend our analysis to other nonlinear oscillators, including more than one oscillator, to quantify the correlation among different oscillators or emergent phenomena, such as synchronisation. This will require solving the Fokker–Planck equation in higher dimensions, which will be computationally challenging, or further developing stochastic simulation methods for an accurate calculation of information geometry diagnostics [40]. Finally, it would be interesting to investigate more general ELM models.

Author Contributions: Conceptualization, E.-j.K.; Methodology, R.H. and E.-j.K.; Software, R.H.; Formal analysis, R.H. and E.-j.K.; Investigation, R.H. and E.-j.K.; Writing—original draft, R.H. and E.-j.K. All authors have read and agreed to the published version of the manuscript.

Funding: E.K. is partly supported by EPSRC Grant EP/W036770/1.

Data Availability Statement: The data that support the findings of this study are available from the corresponding author upon reasonable request.

Conflicts of Interest: The authors declare no conflict of interest.

Appendix A. Complementary Figures

The main text showed results primarily for $\Phi/d = 0.6$ and 1.2 , the smallest and largest values considered. Results for $\Phi/d = 0.8$ and 1.0 may also be of interest though, to show the full range, and how different aspects gradually change. This section, therefore, shows Figures A1–A4 as the equivalents of Figures 3–6, then Figures A5–A8 as the equivalents of Figures 9–12, then Figures A9 and A10 as the equivalents of Figures 13 and 14, and finally Figures A11 and A12 as the equivalents of Figures 15 and 16.

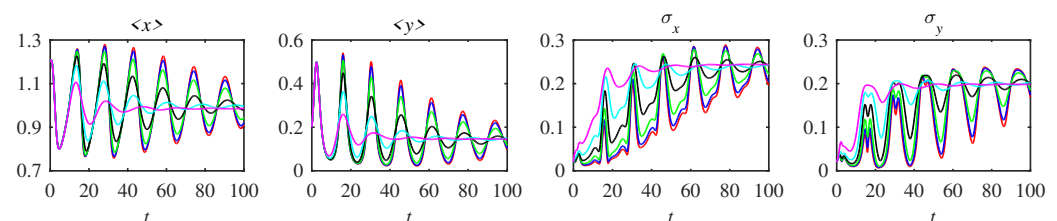


Figure A1. $\Phi/d = 0.8$: Scan over $Q_x = 3 \times 10^{-6}, 10^{-5}, 3 \times 10^{-5}, 10^{-4}, 3 \times 10^{-4}, 10^{-3}$ for $Q_y = 10^{-5}$.

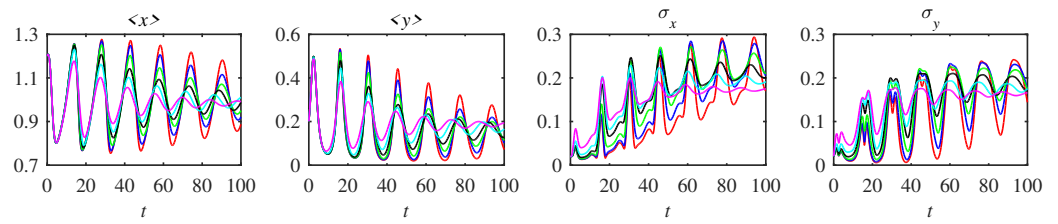


Figure A2. $\Phi/d = 0.8$: Scan over $Q_y = 3 \times 10^{-6}, 10^{-5}, 3 \times 10^{-5}, 10^{-4}, 3 \times 10^{-4}, 10^{-3}$ for $Q_x = 10^{-5}$.

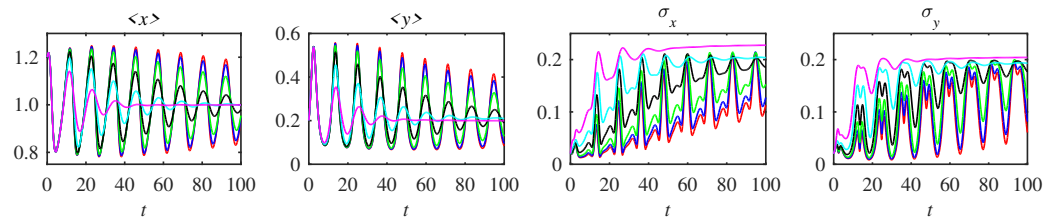


Figure A3. $\Phi/d = 1.0$: Scan over $Q_x = 3 \times 10^{-6}, 10^{-5}, 3 \times 10^{-5}, 10^{-4}, 3 \times 10^{-4}, 10^{-3}$ for $Q_y = 10^{-5}$.

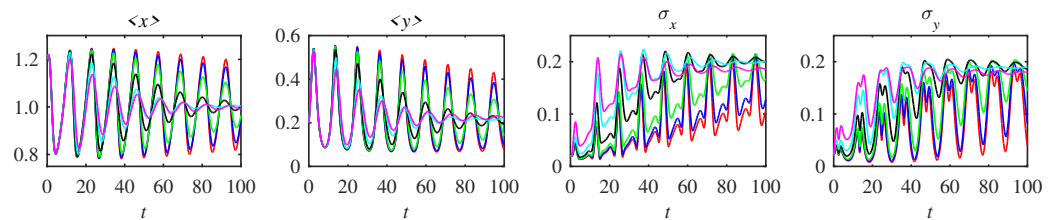


Figure A4. $\Phi/d = 1.0$: Scan over $Q_y = 3 \times 10^{-6}, 10^{-5}, 3 \times 10^{-5}, 10^{-4}, 3 \times 10^{-4}, 10^{-3}$ for $Q_x = 10^{-5}$.

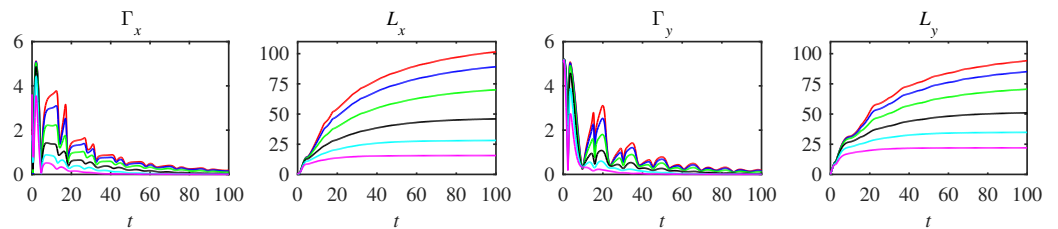


Figure A5. $\Phi/d = 0.8$: Scan over $Q_x = 3 \times 10^{-6}, 10^{-5}, 3 \times 10^{-5}, 10^{-4}, 3 \times 10^{-4}, 10^{-3}$ for $Q_y = 10^{-5}$.

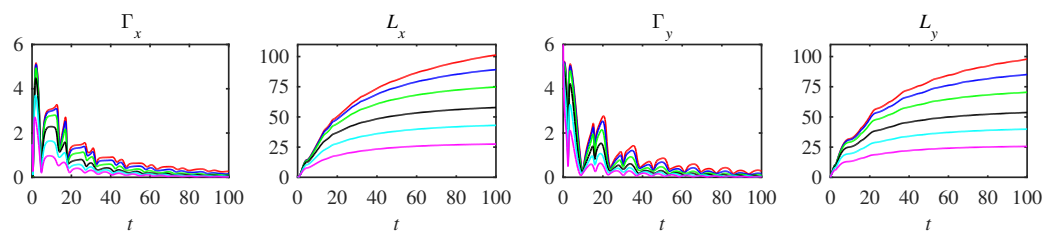


Figure A6. $\Phi/d = 0.8$: Scan over $Q_y = 3 \times 10^{-6}, 10^{-5}, 3 \times 10^{-5}, 10^{-4}, 3 \times 10^{-4}, 10^{-3}$ for $Q_x = 10^{-5}$.

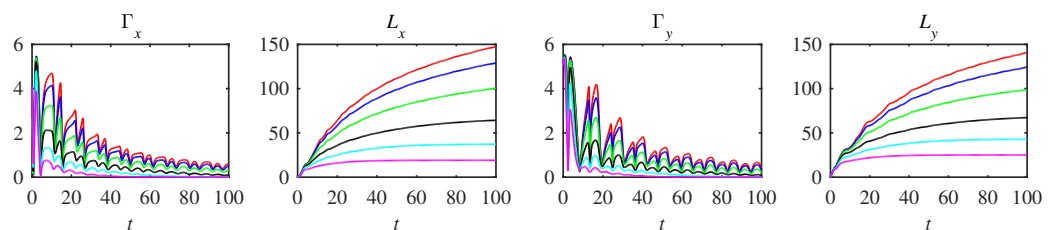


Figure A7. $\Phi/d = 1.0$: Scan over $Q_x = 3 \times 10^{-6}, 10^{-5}, 3 \times 10^{-5}, 10^{-4}, 3 \times 10^{-4}, 10^{-3}$ for $Q_y = 10^{-5}$.

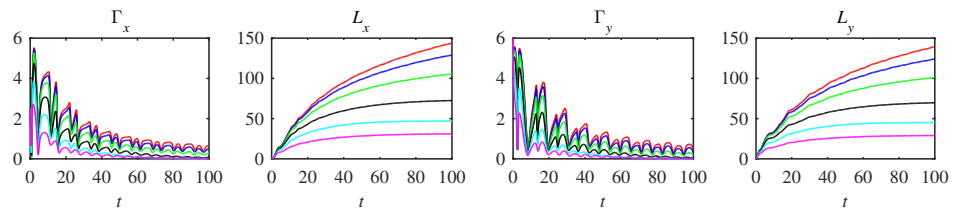


Figure A8. $\Phi/d = 1.0$: Scan over $Q_y = 3 \times 10^{-6}, 10^{-5}, 3 \times 10^{-5}, 10^{-4}, 3 \times 10^{-4}, 10^{-3}$ for $Q_x = 10^{-5}$.

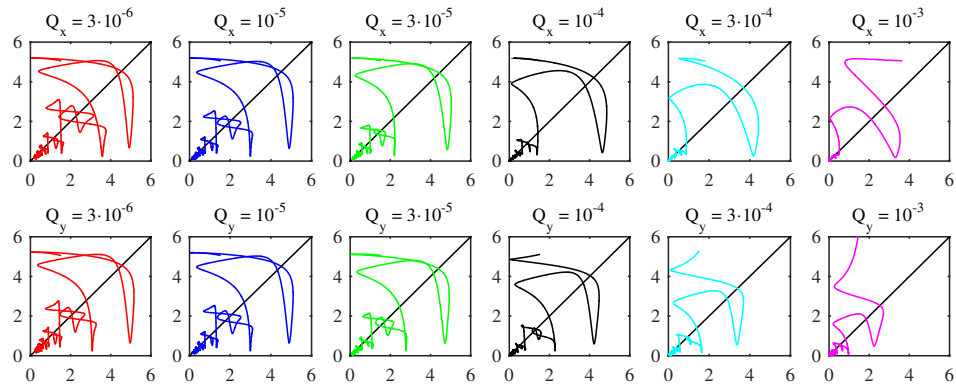


Figure A9. $\Phi/d = 0.8$: Γ_x on the x -axis versus Γ_y on the y -axis. The top row shows scans of Q_x as indicated at fixed $Q_y = 10^{-5}$; the bottom row shows scans of Q_y as indicated at fixed $Q_x = 10^{-5}$.

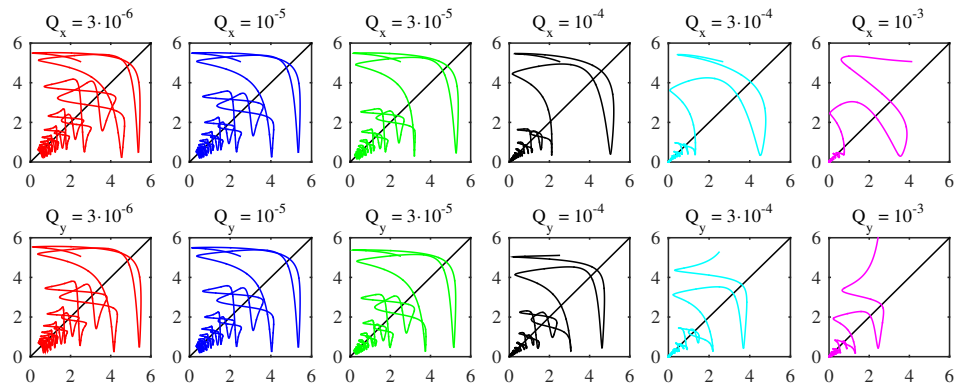


Figure A10. $\Phi/d = 1.0$: Γ_x on the x -axis versus Γ_y on the y -axis. The top row shows scans of Q_x as indicated at fixed $Q_y = 10^{-5}$; the bottom row shows scans of Q_y as indicated at fixed $Q_x = 10^{-5}$.

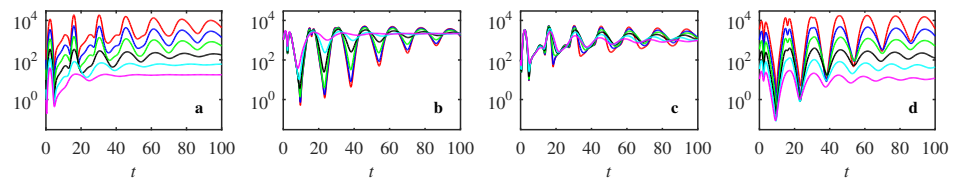


Figure A11. $\Phi/d = 0.8$: Panels (a,b) show \hat{S}_{Tx} and \hat{S}_{Ty} , respectively, as functions of time when scanning over Q_x at fixed $Q_y = 10^{-5}$. Panels (c,d) show \hat{S}_{Tx} and \hat{S}_{Ty} , respectively, as functions of time when scanning over Q_y at fixed $Q_x = 10^{-5}$.

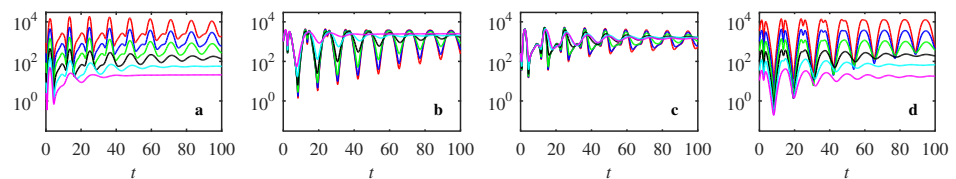


Figure A12. $\Phi/d = 1.0$: Panels (a,b) show \hat{S}_{Tx} and \hat{S}_{Ty} , respectively, as functions of time when scanning over Q_x at fixed $Q_y = 10^{-5}$. Panels (c,d) show \hat{S}_{Tx} and \hat{S}_{Ty} , respectively, as functions of time when scanning over Q_y at fixed $Q_x = 10^{-5}$.

References

1. Benzi, R.; Sutera, A.; Vulpiani, A. The mechanism of stochastic resonance. *J. Phys. A* **1981**, *14*, L453–L457. [[CrossRef](#)]
2. Gang, H.; Nicolis, G.; Nicolis, C. Periodically forced Fokker-Planck equation and stochastic resonance. *Phys. Rev. A* **1990**, *42*, 2030–2041. [[CrossRef](#)]
3. Hollerbach, R.; Kim, E.; Mahi, Y. Information length as a new diagnostic in the periodically modulated double-well model of stochastic resonance. *Phys. A* **2019**, *512*, 1313–1322. [[CrossRef](#)]
4. Simakov, D.S.A.; Pérez-Mercader, J. Noise induced oscillations and coherence resonance in a generic model of the nonisothermal chemical oscillator. *Sci. Rep.* **2013**, *3*, 2404. [[CrossRef](#)]
5. Jaimes-Reátegui, R.; Magallón-García, D.A.; Gallegos, A.; Huerta-Cuellar, G.; García-López, J.H.; Pisarchik, A.N. Noise-induced intermittent oscillation death in a synergetic mode. *Discontinuity Nonlinearity Complex.* **2020**, *9*, 167–172. [[CrossRef](#)]
6. Valenti, D.; Giuffrida, A.; Denaro, G.; Pizzolato, N.; Curcio, L.; Mazzola, S.; Basilone, G.; Bonanno, A.; Spagnolo, B. Noise induced phenomena in the dynamics of two competing species. *Math. Model. Nat. Phenom.* **2016**, *11*, 158–174. [[CrossRef](#)]
7. Haken, H. *Synergetic Computers and Cognition: A Top-Down Approach to Neural Nets*; Springer: Berlin, Germany, 2004.
8. Franci, A.; Herrera-Valdez, M.A.; Lara-Aparicio, M.; Padilla-Longoria, P. Synchronization, oscillator death, and frequency modulation in a class of biologically inspired coupled oscillators. *Front. Appl. Math. Stat.* **2018**, *4*, 51. [[CrossRef](#)]
9. Boccaletti, S.; Pisarchik, A.N.; del Genio, C.I.; Amann, A. *Synchronization: From Coupled Systems to Complex Networks*; Cambridge University Press: Cambridge, UK, 2018.
10. Koseska, A.; Volkov, E.; Kurths, J. Oscillation quenching mechanisms: Amplitude vs. oscillation death. *Phys. Rep.* **2013**, *531*, 173–200. [[CrossRef](#)]
11. Kadomtsev, B.; Laing, E.W. *Tokamak Plasma: A Complex Physical System*; IOP Publishing: Bristol, UK, 1992.
12. Lebedev, V.B.; Diamond, P.H.; Gruzinov, I.; Carreras, B.A. A minimal dynamical model of edge localized mode phenomena. *Phys. Plasmas* **1995**, *2*, 3345. [[CrossRef](#)]
13. Park, H.K.; Lee, J.; Yun, G.S.; Xu, X.Q.; Bécoulet, M. BOUT++ nonlinear simulation for a comparative study with the measured 2D ELM structures in the KSTAR H-mode plasma. *Phys. Plasmas* **2019**, *26*, 052502.
14. Wang, Y.M.; Zu, X.Q.; Yan, Z.; Mckee, G.R.; Grierson, B.A.; Xia, T.Y.; Gao, X. Simulation of density fluctuations before the L-H transition for hydrogen and deuterium plasmas in the DIII-D tokamak using the BOUT++ code. *Nuclear Fusion* **2018**, *58*, 026026. [[CrossRef](#)]
15. Leonard, A.W. Edge-localized-modes in tokamaks. *Phys. Plasmas* **2014**, *21*, 090501. [[CrossRef](#)]
16. Lang, P.T.; Alper, P.; Buttery, R.; Gal, K.; Hobirk, J.; Neuhauser, J.; Stamp, M.; JET-EFDA Contributors. ELM triggering by local pellet perturbations in type-I ELMy H-mode plasma at JET. *Nucl. Fusion* **2007**, *47*, 754. [[CrossRef](#)]
17. Orain, F.; Hoelzl, M.; Mink, F.; Willensdorfer, M.; Bécoulet, M.; Dunne, M.; Günter, S.; Huijsmans, G.; Lackner, K.; Pamela, S.; et al. Non-linear modeling of the threshold between ELM mitigation and ELM suppression by resonant magnetic perturbations in ASDEX upgrade. *Phys. Plasmas* **2019**, *26*, 042503. [[CrossRef](#)]
18. Kirk, A.; Chapman, I.T.; Evans, T.E.; Ham, C.; Harrison, J.R.; Huijsmans, G.; Liang, Y.; Liu, Y.Q.; Loarte, A.; Suttrop, W.; et al. Understanding the effect resonant magnetic perturbations have on ELMs. *Plasma Phys. Control. Fusion* **2013**, *55*, 124003. [[CrossRef](#)]
19. Loarte, A.; Bécoulet, M.; Saibene, G.; Sartori, R.; Campbell, D.J.; Eich, T.; Herrmann, A.; Laux, M.; Suttrop, W.; Alper, B. Characteristics and scaling of energy and particle losses during Type I ELMs in JET H-modes. *Plasma Phys. Control. Fusion* **2002**, *44*, 1815. [[CrossRef](#)]
20. Choi, M.J.; Kwon, J.M.; Kim, J.; Rhee, T.; Bak, J.G.; Shin, G.; Kim, H.-S.; Jhang, H.; Kim, K.; Yun, G.S.; et al. Stochastic fluctuation and transport of tokamak edge plasmas with the resonant magnetic perturbation field. *Phys. Plasmas* **2022**, *29*, 122504. [[CrossRef](#)]
21. Sun, Y.; Liang, Y.; Liu, Y.Q.; Gu, S.; Yang, S.; Guo, W.; Shi, T.; Jia, M.; Wang, L.; Lyu, B.; et al. Nonlinear transition from mitigation to suppression of the edge localized mode with resonant magnetic perturbations in the EAST tokamak. *Phys. Rev. Lett.* **2016**, *117*, 115001. [[CrossRef](#)]
22. Wagner, T.I. The history of research into improved confinement regimes. *Europ. Phys. J. H* **2018**, *43*, 523. [[CrossRef](#)]
23. Diamond, P.H.; Itoh, S.-I.; Itoh, K.; Hahm, T.S. Zonal flows in plasma—A review. *Plasma Phys. Control. Fusion* **2005**, *47*, R35. [[CrossRef](#)]
24. Schmitz, L.; Zeng, L.; Rhodes, T.L.; Hillesheim, J.C.; Doyle, E.J.; Groebner, R.J.; Peebles, W.A.; Burrell, K.H.; Wang, G. Role of zonal flow predator-prey oscillations in triggering the transition to H-mode confinement. *Phys. Rev. Lett.* **2012**, *108*, 155002. [[CrossRef](#)]
25. Kim, E.; Hollerbach, R. Time-dependent probability density functions and information geometry of the low-to-high confinement transition in fusion plasma. *Phys. Rev. Res.* **2020**, *2*, 023077. [[CrossRef](#)]
26. Mlynar, J.; Ficker, O.; Macusova, E.; Markovic, T.; Naydenkova, D.; Papp, G.; Urban, J.; Vlasic, M.; Vondracek, P.; Weinzettl, V.; et al. Runaway electron experiments at COMPASS in support of the EUROfusion ITER physics research. *Plasma Phys. Control. Fusion* **2018**, *61*, 014010. [[CrossRef](#)]
27. Svensson, P.; Embreus, O.; Newton, S.L.; Särkimäki, K.; Vallhagen, O.; Fülöp, T. Effects of magnetic perturbations and radiation on the runaway avalanche. *J. Plasma Phys.* **2021**, *87*, 905870207. [[CrossRef](#)]
28. Kim, E.; Hollerbach, R. Non-equilibrium statistical properties, path-dependent information geometry, and entropy relations in edge-localized modes in fusion plasmas. *Phys. Plasmas* **2022**, *29*, 112302. [[CrossRef](#)]
29. Kowalski, A.M.; Martin, M.T.; Plastino, A.; Rosso, O.A.; Casas, M. Distances in probability space and the statistical complexity setup. *Entropy* **2011**, *13*, 1055. [[CrossRef](#)]

30. Oizumi, M.; Tsuchiya, N.; Amari, S. Unified framework for information integration based on information geometry. *Proc. Natl. Acad. Sci. USA* **2016**, *113*, 14817. [[CrossRef](#)] [[PubMed](#)]
31. Frieden, B.R. *Science from Fisher Information*; Cambridge University Press: Cambridge, UK, 2004.
32. Kim, E. Information geometry, fluctuations, non-equilibrium thermodynamics, and geodesics in complex systems. *Entropy* **2021**, *23*, 1393. [[CrossRef](#)]
33. Heseltine, J.; Kim, E. Comparing information metrics for a coupled Ornstein-Uhlenbeck process. *Entropy* **2019**, *21*, 775. [[CrossRef](#)]
34. Nielsen, M.A.; Chuang, I.L. *Quantum Computation and Quantum Information*; Cambridge University Press: Cambridge, UK, 2000.
35. Sagawa, T. *Thermodynamics of Information Processing in Small Systems*; Springer: Berlin/Heidelberg, Germany, 2012.
36. Roldán, É.; Barral, J.; Martín, P.; Parrondo, J.M.R.; Jülicher, F. Quantifying entropy production in active fluctuations of the hair-cell bundle from time irreversibility and uncertainty relations. *New J. Phys.* **2021**, *23*, 083013. [[CrossRef](#)]
37. Sarazin, Y.; Ghendrih, P. Intermittent particle transport in two-dimensional edge turbulence. *Phys. Plasmas* **1998**, *5*, 4214. [[CrossRef](#)]
38. Tsui, H.Y.W.; Wootton, A.J.; Bell, J.D.; Bengston, R.D.; Diebold, D.; Harris, J.H.; Hershkowitz, N.; Hidalgo, C.; Ingraham, J.C.; Kilpatrick, S.J.; et al. A comparison of edge turbulence in tokamaks, stellarators, and reversed-field pinches. *Phys. Fluids B* **1993**, *5*, 2491. [[CrossRef](#)]
39. Risken, H. *The Fokker-Planck Equation: Methods of Solutions and Applications*; Springer: Berlin, Germany, 2013.
40. Thiruthummal, A.A.; Kim, E. Monte Carlo simulation of stochastic differential equation to study information geometry. *Entropy* **2022**, *24*, 1113. [[CrossRef](#)]

Disclaimer/Publisher's Note: The statements, opinions and data contained in all publications are solely those of the individual author(s) and contributor(s) and not of MDPI and/or the editor(s). MDPI and/or the editor(s) disclaim responsibility for any injury to people or property resulting from any ideas, methods, instructions or products referred to in the content.